Self-assembled heterojunction of metal sulfides for improved photocatalysis

Sovann Khan[a,b,1], Heechae Choi[c,d,1], Donghun Kim[c], Seung Yong Lee[a,b], Qiaohong Zhu[e], Jinlong Zhang[e], Seungchul Kim[a,c,*], So-Hye Cho[a,b,*]

[a] *Division of Nano & Information Technology, KIST School, Korea University of Science and Technology, 217 Gajeong-ro, Yuseong-gu, Daejeon 34113, Republic of Korea*
[b] *Materials Architecturing Research Center, Korea Institute of Science & Technology, 5 Hwarang-ro 14-gil, Seongbuk-gu, Seoul 02792, Republic of Korea*
[c] *Computational Science Research Center, Korea Institute of Science & Technology, 5 Hwarang-ro 14-gil, Seongbuk-gu, Seoul 02792, Republic of Korea*
[d] *Theoretical Materials & Chemistry Group, Institute of Inorganic Chemistry, University of Cologne, Greinstr. 6, 50939 Cologne, Germany*
[e] *Key Laboratory for Advanced Materials and Institute of Fine Chemicals, East China University of Science and Technology, 130 Meilong Road, Shanghai 200237, PR China*

HIGHLIGHTS

- Immiscibility is important in an efficient herojuction photocatalyst.
- Immiscibility of ZnS and NiS were proposed and experimentally proved.
- ZnS-NiS composites showed superior photocatalytic activities.
- Mechanism study explained that NiS plays a role as a co-catalyst of ZnS.

GRAPHICAL ABSTRACT

Self-assembled heterostructure of zinc-nickel sulfides with a highly improved photocatalytic activity.
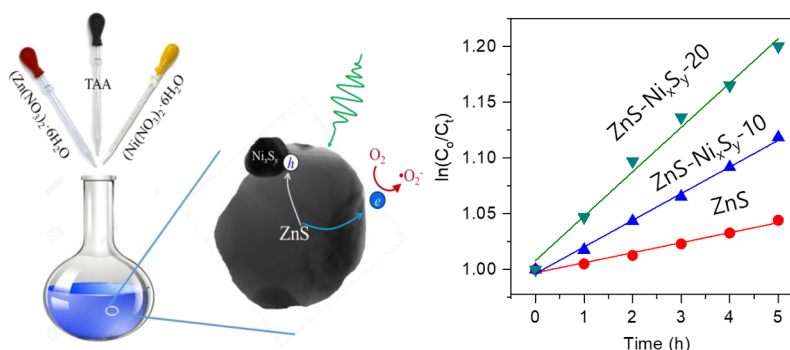
ABSTRACT

Due to its high redox potential, zinc sulfide (ZnS) is considered an excellent semiconductor photocatalyst. However, the rapid recombination rate of the photogenerated electron-hole pairs limits the efficiency of ZnS for photocatalytic reactions. Herein, we suggest a design rule of heterojunction structure of ZnS for improvement of its photocatalytic performance. Two specific properties are specially emphasized: phase immiscibility and the different growth rates of the component materials. The phase immiscibility not only guarantees a well-separated interface, it also enables the technical convenience of one-pot synthesis. The different growth rates help form wide heterojunctions that foster the efficient consumption of materials. We found that the ZnS/Ni_xS_y composite not only meets the aforementioned requirements but also has proper band alignment. Ready-to-use heterojunction photocatalysts (ZnS/Ni_xS_y) were obtained via one-pot synthesis, thanks to the different growth rates and the immiscibility of the two sulfides. Combining ZnS with Ni_xS_y resulted in substantially improved photocatalytic activity in regard to dye decomposition and H_2 production via water splitting. Both band position measurements and DFT simulations indicated that Ni_xS_y is a co-catalyst

* Corresponding authors at: Division of Nano & Information Technology, KIST School, Korea University of Science and Technology, 217 Gajeong-ro, Yuseong-gu, Daejeon 34113, Republic of Korea.
  E-mail addresses: sckim@kist.re.kr (S. Kim), sohyec@kist.re.kr (S.-H. Cho).
  [1] These authors contributed equally.

for ZnS, allowing sufficient band offset for electron-hole separation. Abundant and mass-producible, the ZnS/Ni$_x$S$_y$ composite can effectively substitute for noble metal photocatalysis when it comes to organic pollutant degradation and water splitting.

1. Introduction

ZnS is regarded as an excellent photocatalytic material due to its active reduction power with the deep conduction band edge, which is −1.04 V to the normal hydrogen electrode (NHE), a significant difference when compared to TiO$_2$ photocatalysts (~ -0.2 V to NHE) [1,2]. The direct bandgap of ZnS makes its photoexcitation probability higher than most other indirect bandgap semiconductors [1,3]. However, like many photocatalytic direct bandgap materials, ZnS suffers from a high electron-hole recombination rate. Hence, it is desirable to engineer ZnS in such a way as to efficiently separate photogenerated electron-hole pairs to allow for stronger photocatalytic activity. In general, utilizations of built-in electric fields at the surfaces and/or the creation of heterojunctions with different phases or materials have been suggested as successful methods for suppressing recombination [4–8].

A few recent experimental works have reported that ZnS showed improved photocatalytic activity in a heterojunction with other semiconductors such as C$_3$N$_4$, TiO$_2$ and CdS [9–13]. The origin of the stronger photocatalysis of the heterojunction ZnS is believed to derive from the fast separation of photoexcited electron-hole pairs. However, defects or mixing two materials at the interface could induce recombination centers and limit an activity. In a ZnS/TiO$_2$ heterojunction [10,11], only limited enhancement was observed presumably because Zn substitutes Ti on the TiO$_2$ surface, such that it creates a deep level for charge-carriers to recombine [14]. In a ZnS/CdS heterostructure, in-gap defect levels of ZnS, such as a Zn vacancy, had been suggested to form, acting as trap sites of photogenerated holes [15].

In designing a heterojunction photocatalyst, careful consideration must be given to both electronic structures and chemical properties. The electronic structure of the material junctioned with ZnS requires sufficient band offsets and staggered band alignments (or, for metallic materials, downward band bending of ZnS [i.e., n-type Schottky contact] to utilize the conduction band edge of ZnS). Furthermore, intermixed phases or interface defects must not to be formed to avoid charge-carrier recombination and deformation of the band structure of ZnS. The electronic structure requirement has been thoroughly considered previously, whereas the chemical property requirement has not.

In this study, we carefully consider both the electronic structures and chemical properties in selecting a proper heterojunction material for a ZnS photocatalyst. For the electronic structure, we used density functional theory (DFT) simulations for the band alignment at the junctions. For the chemical property, we used thermodynamic calculations to examine the immiscibility of the material heterojunction with ZnS. Out of several possibilities, we found Ni$_x$S$_y$ to be best suited for the heterojunction material of ZnS—DFT simulations proposed the formation of a Schottky-contact in the ZnS/Ni$_x$S$_y$ interface and a sufficient band offset. Gibbs free-energy calculations suggest phase immiscibility in almost all ZnS/Ni$_x$S$_y$ compositions.

The ZnS/Ni$_x$S$_y$ composites have been previously reported, but it is not yet clear whether the two metal sulfides form a solid solution (Zn$_{1-x}$Ni$_x$S) or an immiscible composite (ZnS/Ni$_x$S$_y$). For example, spontaneous Ni-doping in ZnS by solution methods was considered by Kumar et al. [16] and Kudo et al. [17], but a well separated composite structure of ZnS and NiS was reported by Derikvandi et al. [18] and Wei et al [19]. Du et al. also reported an immiscible composite of three sulfides—CdS, ZnS, and NiS, but they used a consecutive synthesis of each sulfide instead of one-pot reaction to ensure heterojunction formation [20].

To demonstrate the immiscibility of ZnS and Ni$_x$S$_y$ and to conduct kinetic studies, we selected the thioacetamide-mediated solution synthesis of metal sulfides. Analysis of the resulting sulfide product showed that it is a composite with two immiscible phases, ZnS and
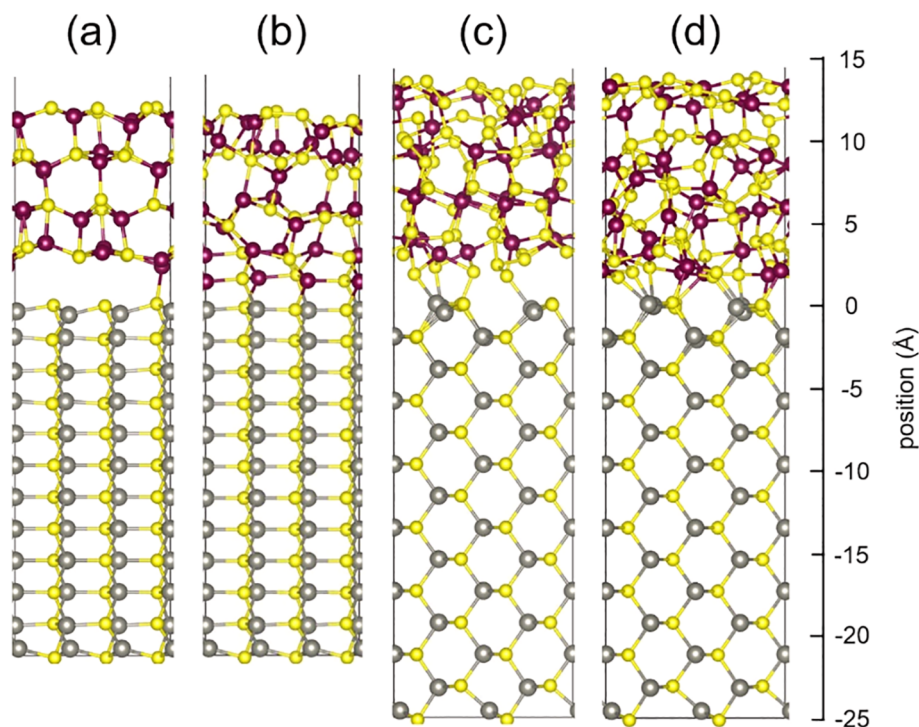

Fig. 1. Atomic structure models of ZnS/Ni$_x$S$_y$ junctions with: (a) crystalline NiS (*c*-NiS); (b) amorphous NiS (*a*-NiS); (c) crystalline NiS$_2$ (*c*-NiS$_2$); and (d) amorphous NiS$_2$ (*a*-NiS$_2$). NiS$_2$ in (c) is crystalline except top-most part. Red spheres are zinc, gray spheres are nickel and yellow spheres are sulfide atoms (for interpretation of the references to colour in this figure legend, the reader is referred to the web version of this article). (For interpretation of the references to color in this figure legend, the reader is referred to the web version of this article.)

Ni_xS_y. The kinetic studies of ZnS and Ni_xS_y formation showed that ZnS grows much faster in the presence of Ni_xS_y, serves as a seed for Ni_xS_y to grow at a later stage of the composite formation and thereby benefitting us in terms of reduced defect formation at the interface. The feasibility of our argument about both electronic structural and chemical property consideration was demonstrated via the photocatalytic activity of the composite for both organic dye degradation and water splitting. When Zn and Ni precursors were mixed in a 4:1 M ratio and reacted in one pot, the resulting heterojunction materials showed a 4–5 times increase in photocatalytic activity compared to ZnS.

Our study provides a design rule for an efficient heterojunction photocatalyst with a special emphasis on the chemical property requirement—suppressing the formation of atomically intermixed phases and defects at the interface since they are often sources for charge recombination and electronic-band deformation.

2. Experimental and computational

2.1. Computational method

Density functional theory (DFT) calculations were performed using Vienna Ab initio Simulation Package (VASP) within the generalized gradient approximation (GGA-PBE) [21,22] to obtain total energy and atomic structures, while the PBE-1/2 method [21,22] was used in the electron density of state (DOS) calculations instead of the PBE for bandgap correction purposes. CUT parameters for PBE-1/2 were 0.881 Å (Zn 3d), 1.794 Å (S 3p) [22] and 1.852 Å (Ni 3d). The bandgap of cubic phase ZnS was calculated to be 3.74 eV [21,22], which is a little larger than experimental value of 3.54 eV. PBE functional predicts atomic structures of ZnS, NiS, and NiS_2 accurately. The limitation of DFT-1/2 is recently discussed especially for covalent semiconductors [23,24], but this method works well for ZnS. We also found that VBM relative to E_F from PBE-1/2 and PBE are almost the same.

Slab geometries in the periodic supercell were used, and a junction model was made to have ZnS and Ni_xS_y in contact. As major compositions of Ni_xS_y were NiS and NiS_2 and both amorphous and crystalline nickel sulfides were observed in our experiment, we modeled crystalline and amorphous structures of both NiS and NiS_2 (Fig. 1). The lateral cell vectors for ZnS/NiS junction were 9.43 and 6.66 Å in length with a cell angle of 90°, and those for ZnS/NiS_2 were 13.33 and 11.54 Å in length with a cell angle of 54.73°. Approximately, 15 Å of vacuum was placed to separate periodic slabs in the perpendicular direction. Since ZnS particles were larger and more crystalline than Ni_xS_y particles in our experiment, we used supercells of un-deformed ZnS, but deformed Ni_xS_y for modeling. The atomic structures were generated combining DFT-MD and structural relaxation, starting from the best fit slab models of Ni_xS_y to ZnS (1 1 0).

Crystalline NiS (c-NiS) structure presented in Fig. 1 (a) was obtained from structural relaxation, while other three structures were generated using DFT-MD simulations followed by structural relaxation. To obtain amorphous NiS (a-NiS) and crystalline NiS_2 (c-NiS_2) models in Fig. 1 (b) and (c), MD simulations were performed for 30 ps at 1000 K, followed by atomic structure relaxation. For atomic structure relaxation of a-NiS_2 (Fig. 1 (d)), we conducted successive MD simulations by adding small amount of NiS_2 (24 atoms) at each step; at first, MD simulations were run with 8 units of NiS_2 on the ZnS slab for 10 ps, then 8 more units were added before second MD calculations. This process was repeated four times. There was a strong repulsion between ZnS (1 1 0) and bulk-truncated c-NiS_2, as the outer most ions are S ions for both ZnS and NiS_2, which resulted more complicated process to generate the contact between ZnS and NiS_2 than to generate the contact between ZnS and c-NiS. For example, simple relaxation using bulk-truncated ZnS and NiS_2 without high temperature MD did not provide any bond formation and hence DFT-MD simulations were performed at 1000 K for 30 ps using SIESTA code [25].

2.2. Synthesis method

ZnS, ZnS/Ni_xS_y, and Ni_xS_y particles were synthesized by a hydrothermal method since it is known to be applicable for the synthesis of crystalline nanoparticles of sulfides [26]. A total of 0.01 mol of metal nitrate hexahydrates ($Zn(NO_3)_2·6H_2O$ and $Ni(NO_3)_2·6H_2O$, Aldrich Inc., USA) and 0.01 mol of thioacetamide, (TAA, CH_3CSNH_2, Daejung Chemical Inc., South Korea) were dissolved in 50 mL of de-ionized water and stirred with a magnetic stirrer for 2 h. Concentrations of Ni precursor were varied by 0, 10, 20, and 30 mol% of the total concentration of metal precursors, each of which is denoted as Ni-0, Ni-10, Ni-20 and Ni-30 in the text. For comparison, single component ZnS and Ni_xS_y was also synthesized by the same method and designated Ni-0 and Ni-100 in the text. The resulting transparent solution was transferred into a 100-mL Teflon-lined stainless-steel autoclave, which was then placed in a furnace maintained at 200 °C for 4 h. The obtained precipitates were isolated by centrifugation, washed with de-ionized water three times, and dried in an oven at 60 °C for 24 h. The dried powder was used for characterization and photocatalysis without any further treatment.

For examination of the growth kinetics, an equimolar mixture of Zn $(NO_3)_2·6H_2O$ (0.01 mol) and $Ni(NO_3)_2·6H_2O$ (0.01 mol) and thioacetamide (0.02 mol) were dissolved in 50 mL of de-ionized water and subjected for the hydrothermal reaction as described above. Relative yields (%) and compositions (%, Zn and Ni) of ZnS/Ni_xS_y composites were recorded as a function of reaction times (20, 40, and 60 min) and compared with those of single component ZnS and Ni_xS_y.

2.3. Photocatalytic activity measurement

Organic dye degradation: 20 mg of sulfide composite was taken and well dispersed into a 50-mL aqueous solution of eosin B (4.5×10^{-6} M in de-ionized water, Sigma Aldrich Inc., USA) by sonication in darkness. The mixture was then placed under a UV light (UV-B lamp, G15T8E, Sankyodenki, Japan) with continuous stirring by a magnetic stirrer at 400 rpm. After a predetermined time, 3 mL of the mixture was taken and immediately centrifuged (10,000 rpm, 10 min) to remove the composite to stop the catalytic reaction. The amount of remaining eosin B after the photocatalytic degradation was determined by the intensity of the UV/vis absorption at λ = 521 nm based on a calibration curve made with a reference solution of eosin B [27]. For trapping experiment, each scavenger, benzoquinone (BQ, Aldrich Inc., USA, 0.05 mM), isopropyl alcohol (IPA, Daejung Chemical Inc., South Korea, 0.1 mM), and ammonium oxalate monohydrate (AMO, Aldrich Inc., USA, 0.5 mM), was added to the aqueous solution of eosin B (50 mL) containing Ni-0 or Ni-20 sulfide catalyst (20 mg) and the eosin B degradation was monitored by the same manner.

For a recycling test, the colloidal solution was prepared in the same manner and exposed to the light source for 5 h with stirring. The used catalyst was isolated by centrifugation and dispersed again in the freshly-prepared eosin B solution. The colloidal solution was subjected for eosin B degradation in the same manner as the 1st cycle. The repeat experiments were conducted up to 5st cycle and amounts of remaining eosin B were determined by the intensity of the UV/vis absorption.

Hydrogen production via water splitting: For hydrogen evolution, 50 mg of a sulfide composite was dispersed in a 100-mL aqueous solution containing 0.1 M Na_2S and 0.1 M Na_2SO_3 as hole scavenger [1]. The mixture was placed in a 200-mL glass reactor equipped with a water circulator for cooling, then tightly covered with a quartz window. The reactor was evacuated for 30 min to remove any residual air before being subjected to light irradiation using a solar simulator equipped with the AM1.5 filter. The hydrogen gas that evolved during the photocatalysis was collected in the glass reactor and intermittently subjected to a gas chromatography (GC) connected to the reactor. A GC calibration curve for hydrogen was obtained using hydrogen reference samples.

For a recycling test, the colloidal solution was prepared in the same

manner and exposed to the light source for 4 h. The used catalyst was isolated by centrifugation and dispersed again in the freshly-prepared electrolyte solution. The colloidal solution was subjected for water splitting in the same manner as the 1st cycle. The repeat experiments were conducted up to 3rd cycle and produced hydrogen was measured by GC.

The apparent quantum efficiency of hydrogen production was determined via the standard method [28]. The wavelength of light for the efficiency measurement was 365 nm, the optical power was 15.7 mW/cm^2, and the irradiated area was 43.0 cm^2.

2.4. Characterizations

Structural properties of the synthesized powder were analyzed by scanning electron microscopy (SEM) (Nova-SEM, FEI Company, USA), high-angle annular dark-field (HAADF) imaging, selected area electron diffraction (SAED), and high-resolution-transmission electron microscopy (HR-TEM) (Talos F200X, FEI Company, USA). Powder X-ray diffraction (XRD) data were collected at room temperature using a Rigaku DMAX-2500PC with graphite-monochromatized Cu-Kα radiation (λ = 1.5418 Å) in the 2θ range 10 to 145° with a step size of 0.01°. The voltage and electric current were held at 40 kV and 200 mA. Rietveld refinements and quantitative analyses were performed using the TOPAS5 program with modified pseudo-Voigt peak shapes and refined backgrounds by Chebychev function. The compositional properties were analyzed by elemental mapping using energy-dispersive X-ray spectroscopy (EDS) (Talos F200X, FEI Company, USA) and an atomic absorption spectrometer (AAS) (ICE3000, Thermo, USA). The optical properties were obtained using a UV–visible spectrophotometer (Varian Cary 100, Agilent Technologies, USA). Hydrogen evolution was monitored by gas chromatography (6500 GC system, YL instrument, South Korea) outfitted with a thermal conductive detector (TCD) and a 5-Å molecular sieves column. Valence band positions and work functions of sulfides were obtained by X-ray photoelectron spectroscopy (XPS) and Ultraviolet photoelectron spectroscopy (UPS) (PHI 5000 Versa Probe, ULVAC PHI, Japan). Binding energies of Zn 2p and Ni 2p were also obtained by XPS using the same instrument.

3. Results and discussion

At the first stage of the research, we tested immiscibility of five metal sulfides (CdS, MgS, NiS, PbS and SnS) with ZnS by Gibbs free energy calculations of mixed composites. Two sulfides, NiS and CdS, were found to be immiscible with ZnS (Supplementary Info., Fig. S1), but we excluded CdS in this study not only because it contains a toxic element but also ZnS/CdS forms a straddling band alignment with ZnS such that it traps both electrons and holes [15]. On the other hand, NiS was more desirable since it forms a staggered band alignment with ZnS

and has a sufficiently different formation enthalpy from that of ZnS (standard formation enthalpy of ZnS is −204.6 kJ/mol [26] and that of NiS is −87.86 kJ/mol [21]), which benefits for ideal growth of heterojunctions.

For the Gibbs free energy of ZnS/NiS mixing (ΔG_{mix}), 450 K and 1100 K were chosen as representative temperatures for low and high temperature procedures, respectively, and the calculation was done using the equation:

$$\Delta G_{mix} = \Delta H_{mix} + T\Delta S_{mix} \qquad (1)$$

where ΔH_{mix} and ΔS_{mix} are the enthalpy and entropy change by ZnS/NiS mixing in bulk, respectively. The ΔH_{mix} term is obtained from the DFT total energy difference with varying NiS fraction, x, for reactions:

$$(1 - x)ZnS + xNiS \rightarrow Zn_{(1-x)}Ni_xS \qquad (2)$$

To calculate ΔS_{mix}, we considered only the configurational entropy of random mixing, since the contributions of vibrational entropy are largely cancelled out in calculation for bulk matter. The ΔS_{mix} term for configurational change in $Zn_{(1-x)}Ni_xS$ is expressed as

$$\Delta S_{mix} = k_B[x\ln x + (1 - x)\ln(1 - x)] \qquad (3)$$

At T = 450 K, ΔG_{mix} is positive over all NiS fractions, due to a high positive ΔH_{mix} value (Fig. 2(a)). At T = 1100 K, the calculated ΔG_{mix} becomes close to zero with very low fractions of NiS (< 0.2) and turns negative with 0.92 or larger fractions of NiS, which means that mixing of two phases is only allowed when one is present at a much lower level than the other (Fig. 2(b)). Atomic doping energies were also calculated for Zn(Ni)-doping in NiS (ZnS). A doping energy is the change of Gibbs free energy of the system affected by doping an alien atom in a dilute limit. Therefore, once the doped atom is considered as a defect, an atomic doping energy is identical to a defect formation energy. The energy of substitutional doping was calculated to be 1.4 eV/atom for Zn into NiS, and 0.6 eV/atom for Ni into ZnS, indicating that the atomic doping is also endothermic. Therefore, we expect formation of well-separated heterojunction of ZnS and NiS phases under our reaction conditions in terms of thermodynamic immiscibility. The above-mentioned work by Kudo et al. [17] can also be explained by our calculation results – they obtained the Ni-doped ZnS when they used an extremely low mole fraction of Ni (0.001) at a relatively high temperature (775 K). Experimental validation of our idea was followed after computational screening.

ZnS/NiS composite materials were obtained by the hydrothermal process and their XRD patterns are presented in Fig. 3. A well-crystalline cubic phase of ZnS (c-ZnS) was observed for pure ZnS (Ni-0) – major peaks were found at 28.45, 33.00, 47.45, 56.25 and 59.00°, which can be indexed to the plane (1 1 1), (2 0 0), (2 2 0), (3 1 1) and (2 2 2) of c-ZnS (JCPDS#-01-071-5976), respectively (Fig. 3). Minor peaks were also found at 27.25 and 30.77° which can be indexed for
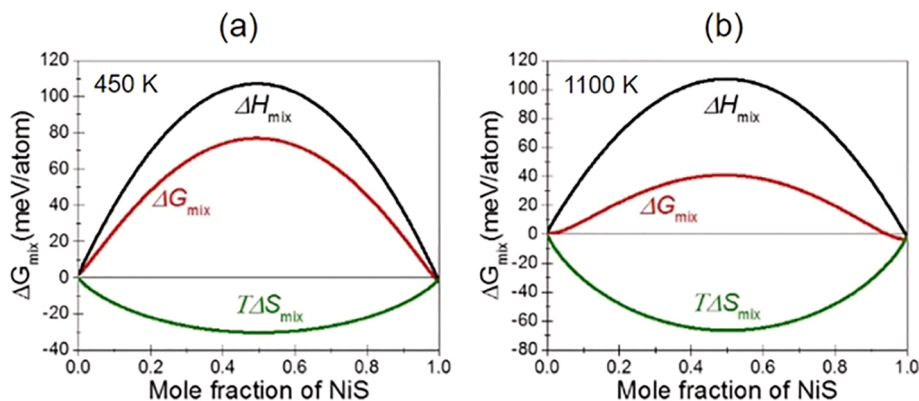

Fig. 2. Calculated ΔH_{mix}, ΔS_{mix}, and ΔG_{mix} of ZnS/NiS solid solutions as a function of the relative mole fractions of NiS at two different temperatures (T = 450 K and 1100 K).
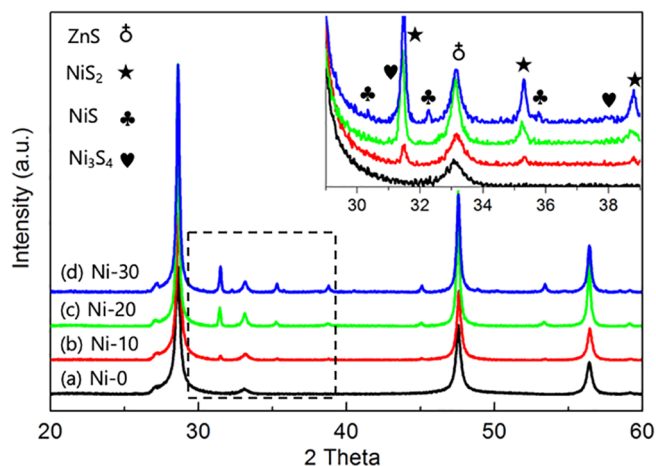
Fig. 3. XRD spectra of (a) Ni-0; (b) Ni-10; (c) Ni-20; (d) Ni-30.

hexagonal ZnS (*h*-ZnS, JCPDS#80-0007). It is known that *c*-ZnS structure has slightly lower energy than *h*-ZnS at standard temperature and pressure (at 298 K and 1 bar) while *h*-ZnS is more stable above 1020 °C [29]. Therefore, typical solution-phase synthesis of ZnS provide *c*-ZnS preferentially [2] and we also found *c*-ZnS as a major product by the hydrothermal method. For all Ni-contained samples, XRD peaks of *c*-ZnS were clearly appeared, along with small peaks corresponding to Ni_xS_y phases. The magnified XRD spectra at the range of 29-39°, shown in the inset of Fig. 3, revealed multi-phases of the nickel sulfide such as NiS_2 (JCPDS#01-078-4702), Ni_3S_4 (JCPDS#00-047-1739) and NiS (JCPDS#00-012-0041). Unlike to findings by Kumar et al. that a shift of ZnS XRD peaks towards higher angle occurred with increasing Ni doping from 1 to 5 mol% [16], we did not observe any shift of ZnS main peak of (1 1 1) plane upon mixing with nickel sulfides, which indicates a low possibility of Ni-alloying to ZnS. We tried to obtain nickel sulfide with a high phase purity by varying the concentration of nickel and sulfur precursors, but it was not successful. Karthikeyan et al. have used a similar hydrothermal process for the synthesis of nickel sulfide, and they also reported a mixed phase of NiS, NiS_2, $Ni_{17}S_{18}$, and Ni_3S_4 [26].

Rietveld analysis of Ni-containing samples were further performed to precisely identify phases of Ni_xS_y and evaluate ratios of each (Fig. 4). For Ni-10, two phases—NiS_2 and Ni_3S_4—were found in the relative ratios of 3.11 and 0.36 at.%, respectively, while with Ni-20 and Ni-30, three phases—NiS_2, Ni_3S_4 and NiS—were found in the relative ratios of 8.67, 0.18 and 0.07 at.%, (Ni-20), and 13.23, 1.11, and 1.39 at.% (Ni-30), respectively. The existence of different oxidation states of Ni in Ni_xS_y (oxidation states of Ni are +4.0, +2.7, and +2.0 in NiS_2, Ni_3S_4, and NiS, respectively) was also confirmed by multiple surface valence states of Ni 2p for Ni-30 discovered through XPS analysis (Supplementary Information, Fig. S2). Peak fitting of Ni 2p binding energies for Ni-30 revealed two peaks (853.8 and 871.5 eV) and two shake-up satellite peaks (859.8 and 881.6 eV), corresponding to the Ni^{2+} valence state. Additionally, broad peaks were found at slightly higher binding energies than the Ni^{2+} valence state, 855.5 and 875.8 eV, which are associated with oxidized valence states of Ni^{2+} [30]. On the other hand, the Zn 2p XPS spectrum for Ni-30 showed clear 2p3/2 and 2p1/2 doublets at 1022.4 eV and 1045.3 eV, closely matching up with that for Ni-0. Therefore, it is worth considering that the oxidation of Ni^{2+} is not related to Zn^{2+} chemical sources in the reaction mixture but rather to its susceptibility to air oxidation under harsh conditions such as hydrothermal reaction [26,31].

To confirm the compositional information suggested by the Rietveld refinement of XRD spectra, 3.47, 8.92, and 15.73 at.% of Ni_xS_y among all sulfides for Ni-10, Ni-20 and Ni-30, respectively, we performed an atomic absorption spectrometry (AAS) measurement. As shown in Table 1, AAS revealed nickel composition of 3.17, 10.36 and 17.99 at.%

for Ni-10, Ni-20 and Ni-30, respectively. Although the AAS values are similar to those obtained by XRD, nickel values in AAS are higher than those in XRD for both Ni-20 and Ni-30. This discrepancy originates due to only crystalline phases being counted in XRD. Therefore, the lower compositional values of Ni_xS_y in XRD imply the existence of amorphous and other minor phases of nickel sulfides.

The compositional analysis showed that Ni_xS_y formation is substantially lower than expected, likely due to lower rates of its formation. In fact, the color of the solution after the hydrothermal reaction remained green (the color of Ni precursor), indicating that Ni_xS_y formation was not completed within the span of our reaction time (4 h). Therefore, we performed a kinetic study of metal sulfide formation with an equimolar mixture of Ni and Zn nitrates and single component phases (ZnS and Ni_xS_y) (Fig. 5). In a very early stage of reaction, the growth of ZnS was slightly faster than that of Ni_xS_y in each single component reaction. However, the growth of ZnS in the mixed nitrate solution was noticeably accelerated while that of Ni_xS_y was suppressed so that only ZnS was found in 20 min from the mixed nitrate solution. The development of Ni_xS_y phase notably took off once ~50% of Zn precursors were consumed (see the growth of Ni_xS_y from 40 min to 60 min of reaction).

To check whether it is a general growth property of ZnS/Ni_xS_y composites, not relying on specificity of reaction conditions, we
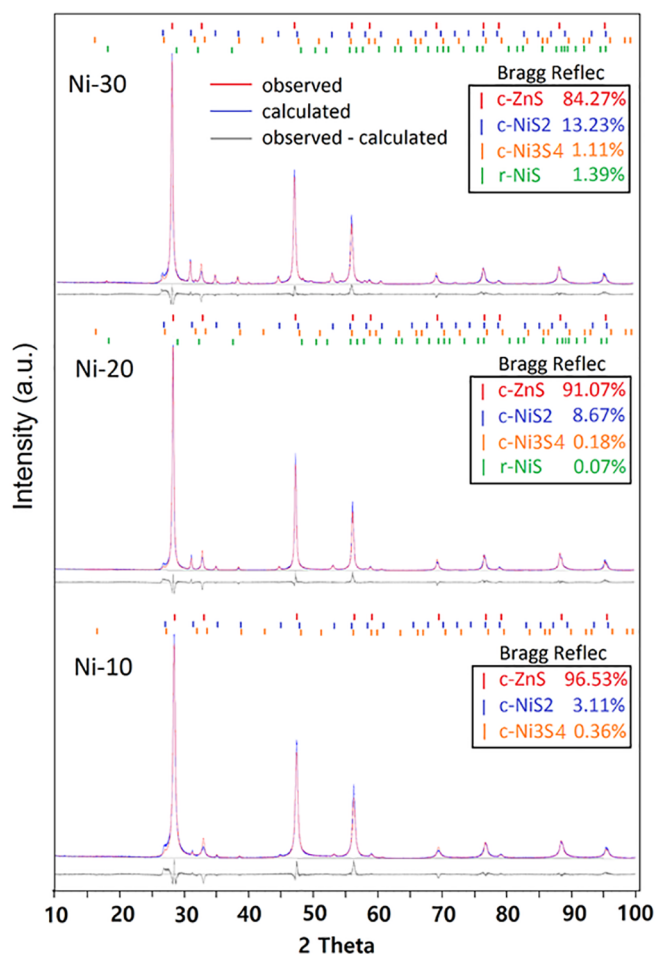

Fig. 4. Rietveld refined XRD patterns of Ni-10; Ni-20; and Ni-30 and their calculated compositions. Spectra were fitted with standard JCPDS # 01-071-5976 (red), 01-078-4702 (blue), 00-047-1739 (orange) and 00-012-0041 (green) for ZnS, NiS_2, Ni_3S_4 and NiS, respectively (for interpretation of the references to colour in this figure legend, the reader is referred to the web version of this article). (For interpretation of the references to color in this figure legend, the reader is referred to the web version of this article.)

Table 1
Theoretical, AAS, and XRD-measured compositions of Ni-10, Ni-20 and Ni-30 in atomic percent (at.%).

Sample	Theoretical		AAS		XRD
	Zn	Ni	Zn	Ni	Ni_xS_y*
Ni-10	90	10	96.83	03.17	3.47 (3.11, 0.36, 0)
Ni-20	80	20	89.64	10.36	8.92 (8.67, 0.18, 0.07)
Ni-30	70	30	82.01	17.99	15.73 (13.23, 1.11, 1.39)

* The values in the parenthesis are atomic compositions of NiS_2, Ni_3S_4, and NiS, in order.

performed precipitation synthesis of the sulfide composite. Analysis on the precipitated sulfides revealed the similar trend: the growth of ZnS was accelerated in the presence of Ni precursors but that of Ni_xS_y was suppressed in the presence of Zn precursors (Supplementary Information, Fig. S3). We did not carry out further studies to understand growth mechanism of the composites because it is not the scope of current paper. However, this kinetic study informed us that two metal sulfides in the composite have highly different growth rates affording less chance of forming a solid solution. Hence, it is reasonable to assume that ZnS nucleates first and grows as single component particles while Ni_xS_y nucleates later, presumably on the surface of ZnS particles since it is energetically more favorable than in the free standing space due to energy gaining by interface binding, and then fast grows into particles. These different growth rates of the two sulfides also benefit for reduced defect formation at the interface.

Morphological observation of the metal sulfides with different nickel concentrations were performed by SEM (Fig. 6). Single-component ZnS (Ni-0) showed an irregular morphology with a rough surface, and its average particle size was approximately 130 nm in diameter (Fig. 6(a)). The particle size increased upon the addition of Ni, almost doubling in size (~250 nm) with the 20 mol% addition of the Ni precursor (Fig. 6(c)). Ni-30 showed a similar particle size as Ni-20, but its surface appeared smoother than the other samples, which may suggest

that the Ni ions (at the high concentration) play a role as a flux material to increase the crystallinity of ZnS, which is in agreement with the XRD data, where peaks of ZnS in Ni-30 was significantly sharper than those in Ni-0.

The SEM images did not make it clear whether the particles were a solid solution of binary metal sulfides or an aggregated composite of two different metal sulfides. Therefore, Ni-20 was examined through TEM and HR-TEM (Fig. 7). A low magnification HAADF-TEM image showed that the particles were an aggregate of smaller crystallites, some of which had highly facetted shapes (marked by red circles in Fig. 7(a)). HADDF and EDS images proved that there are two immiscible phases, which are Ni_xS_y and ZnS (Fig. 7(a) and (b)). SAED patterns for the sulfides informed that they are highly crystalline (insets of Fig. 7(c): the lattice distance of ZnS was ~0.311 nm, which matches up well with JCPDS value of plane (1 1 1) of cubic ZnS (#01-071-5976), while that of Ni_xS_y was ~0.313 nm, which corresponded to JCPDS value of (1 1 1) plane of NiS_2 (#01-078-4702)) but HR-TEM image revealed that the interface has an amorphous layer.

Although the content of Ni_xS_y in Ni-20 is over ~9 at.% according to AAS and XRD analysis, it was difficult to locate many Ni_xS_y particles by TEM, probably because most Ni_xS_y exists as either amorphous phases or nanoparticles too small to be detected by TEM. In fact, our DFT simulation given in Session 2.1 indicates the difficulty of forming an interface of c-ZnS/c-NiS or c-ZnS/c-NiS$_2$ compared to that of c-ZnS/a-NiS or c-ZnS/a-NiS$_2$ (Fig. 1) and hence it is plausible that most Ni_xS_y nucleates on the surface of ZnS as an amorphous phase. We obtained a composite sample with a higher nickel content of 50% (Ni-50) in an effort to prove the immiscibility of ZnS and Ni_xS_y and uniformity by TEM analysis. EDS mapping of Ni-50 at a low magnification (5000×) showed that ZnS and Ni_xS_y are immiscible and the composites are quite uniform throughout the sample and TEM images at higher magnifications revealed that most, but not all, particles constituted heterojunctions, which include a thin amorphous layer between crystalline sulfides (see Supplementary Information, Fig. S4).

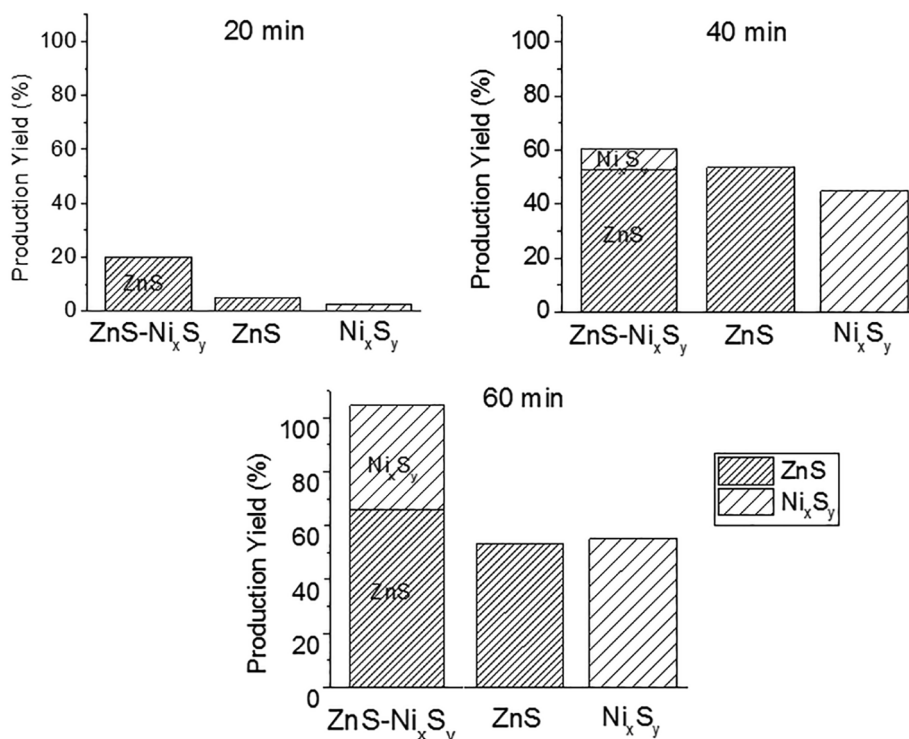To examine if there was any band gap change upon the addition of

Fig. 5. Development of sulfide phases in different reaction times: 20 min, 40 min, and 60 min. ZnS/Ni_xS_y infers the composite product formed from an equimolar mixture of Ni and Zn nitrate precursors and ZnS and Ni_xS_y infer the single component product of ZnS and Ni_xS_y.
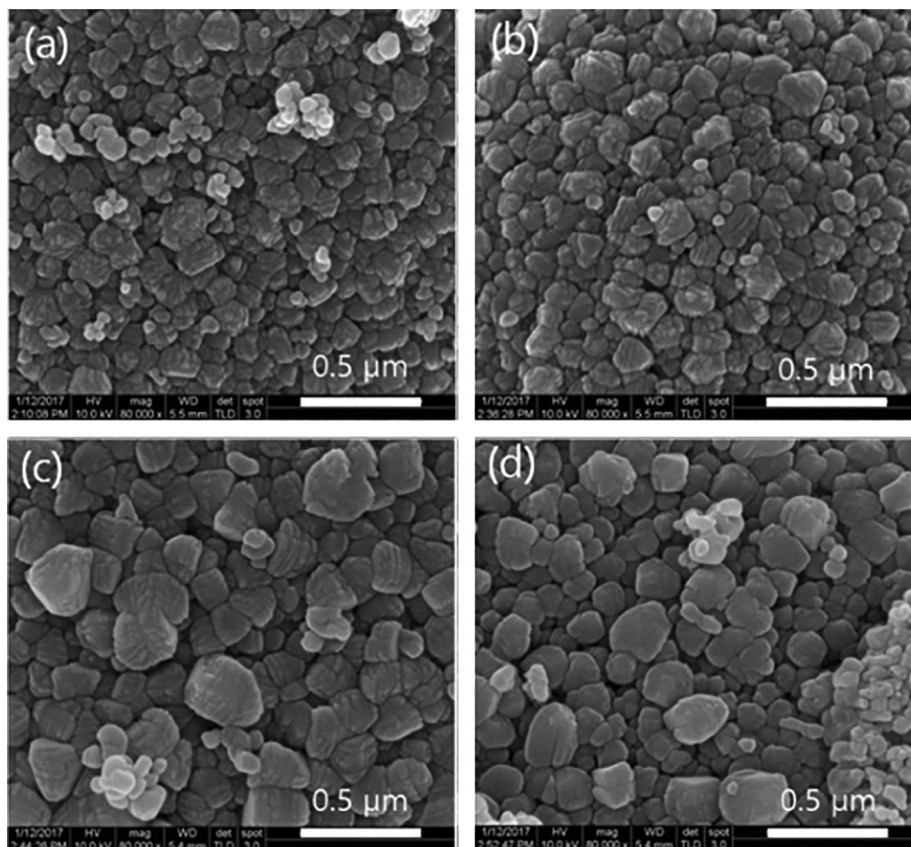
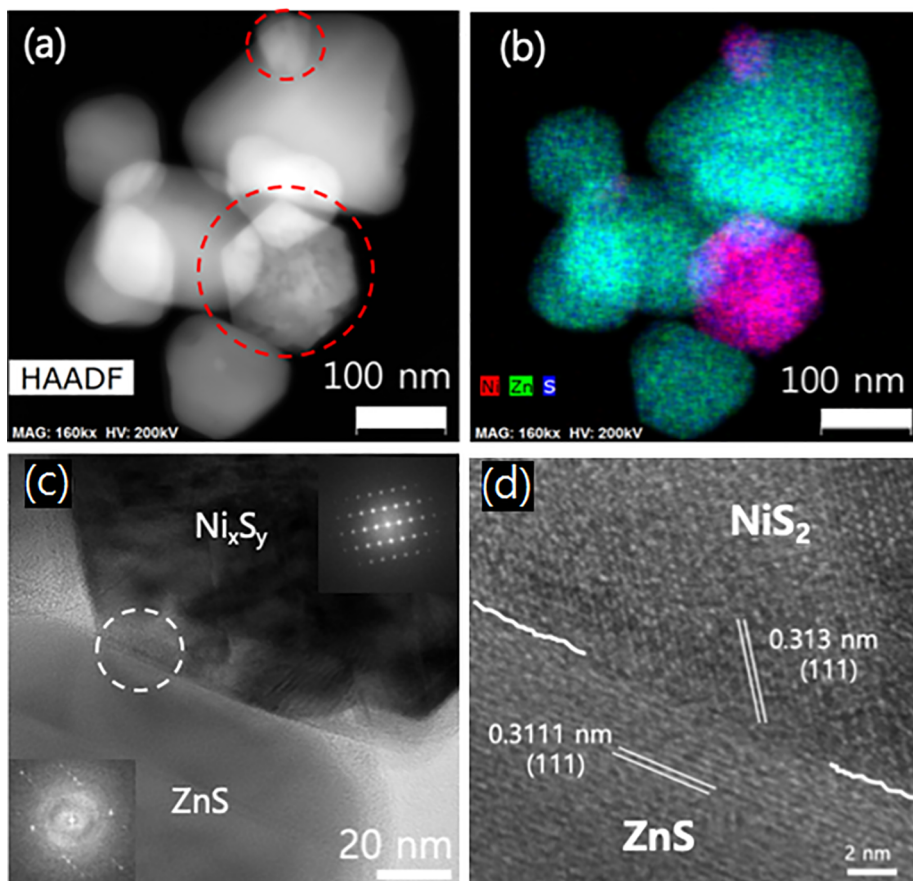**Fig. 6.** SEM images of (a) Ni-0; (b) Ni-10; (c) Ni-20; (d) Ni-30.

Fig. 7. Morphological and elemental characteristics of Ni-20 examined by (a) HAADF-TEM image; (b) elemental mapping image of Zn (green), Ni (red) and S (blue); (c) TEM image at the interfaces of ZnS/Ni_xS_y (insets: SAED patterns of ZnS and NiS_2); (d) HR-TEM image of Fig. 7(c) (the amorphous layers were marked with white lines). For interpretation of the references to colour in this figure legend, the reader is referred to the web version of this article. (For interpretation of the references to color in this figure legend, the reader is referred to the web version of this article.)
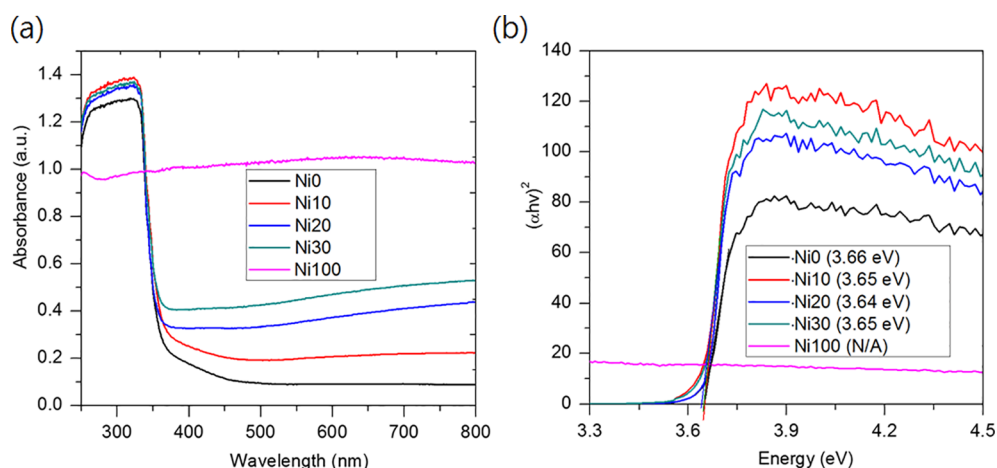
Fig. 8. (a) UV/vis absorption spectra and (b) Tauc plots of Ni-0, Ni-10, Ni-20, Ni-30 and Ni-100.

Ni_xS_y to ZnS, the diffuse reflectance spectra of ZnS/Ni_xS_y sulfide composites were obtained and compared with those of single-component ZnS (Fig. 8(a)). Strong absorptions in the UV range, with an absorption edge at ~360 nm, were observed for all samples containing ZnS, which were associated with the intrinsic band gap absorption of cubic ZnS (3.68 eV) [2]. A broad shoulder peak at 360–460 nm was observed with both Ni-0 (ZnS) and Ni-10, which can be assigned to defect absorptions, typically caused by anion vacancy or dislocation, of the ZnS nanoparticles [32]. As abovementioned, the presence of Ni drives the increased crystallinity of ZnS, which results the decreased defect absorptions of Ni-20 and Ni-30. With an increase of the Ni contents in the metal sulfide, the baseline absorption ranging from 400 to 800 nm

increased, which can be attributed to the photoabsorption of the metallic nickel sulfide, as also proven by the absorption spectrum of Ni-100. Similar trends were also reported with NiS-modified TiO_2 photocatalysts [33,34]. The absorption edge of ZnS was not altered by the addition of Ni, which strongly supports our argument that the samples consisted of two immiscible phases, rather than a solid solution of nickel and zinc sulfides. It should also be noted that in the work by Kudo et al. [17] where the band edge change was described by Ni doping of ZnS ($Zn_{0.999}Ni_{0.001}S$), the Ni doping was done in a very low concentration and at a high temperature (773 K) [34].

Band gap energies (E_g) calculated following the previous study [27] were 3.66, 3.65, 3.64, and 3.65 eV for Ni-0, Ni-10, Ni-20 and Ni-30,
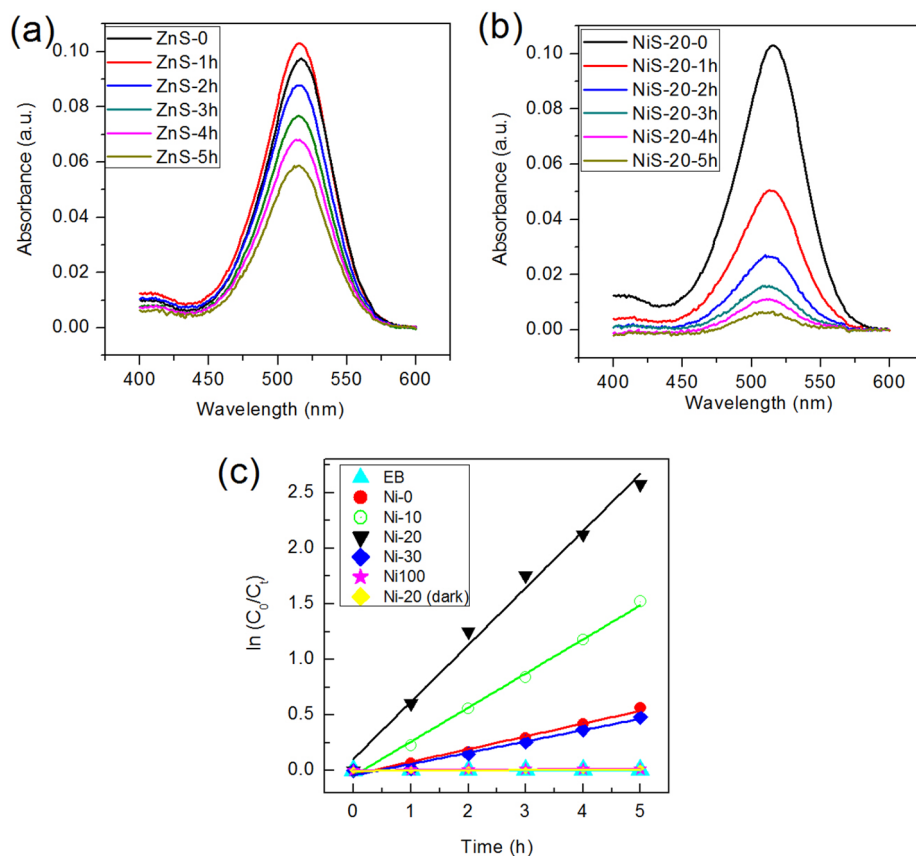

Fig. 9. Photodegradation of eosin B under UV light (a) by pure ZnS (Ni-0); (b) by Ni-20; (c) natural logarithmic plots of C_o (initial concentration of eosin B) over C_t (concentration of eosin B at the time t) as a function of time (h).

respectively (Fig. 8(b)), indicating almost no changes in the band gap energy of ZnS upon addition of NiS. Based on our analysis through XRD, TEM and UV–visible absorption, it is strongly believed that Ni_xS_y and ZnS do not form a solid solution under the given synthetic condition.

The photocatalytic activities of the ZnS/Ni_xS_y composite were first evaluated through de-coloration of eosin B in an aqueous solution. When the ZnS was used, the eosin B slowly degraded as the illumination time increased (Fig. 9(a)), whereas when Ni-20 was used in the same amount, the eosin B degraded much faster (Fig. 9(b)). The comparison of photocatalytic activities of all samples was performed by plotting ln (C_o/C_t) versus reaction times, where C_o and C_t are the concentrations of eosin B at an initial stage and at the reaction time, t (Fig. 9(c)). The eosin B concentration was unchanged under UV light illumination without any sulfide particles and the single-component Ni_xS_y (Ni-100) showed a negligible activity. However, the composite sulfides (Ni-10 and Ni-20) showed distinctively higher activities than the single-component sulfide (Ni-0). The observed activity of composite sulfides was proven to be photocatalytically induced since no activity was observed in darkness. To quantitatively compare the composite and the single-component sulfides, rate constants (k) for the eosin B degradation were obtained from a first order equation (Eq. (4)). The slopes of the plots in Fig. 9(c) represent the rate constants.

$$ln(C_t/C_o) = -kt \qquad (4)$$

The rate constants of single component sulfides, Ni-0 (ZnS) and Ni-100 (Ni_xS_y), were 0.115, and 0.003 h^{-1}, respectively. However, those of composite sulfides, Ni-10 and Ni-20, increased to 0.307 and 0.513 h^{-1}, respectively. Ni-30 exhibited a rather reduced activity than those shown by Ni-10 and Ni-20, exhibiting a rate constant of 0.102 h^{-1}. The reduced activity of Ni-30 could be due to a light-shielding effect of Ni_xS_y. As we witnessed the significant light absorption in the UV range (Fig. 8(a)) and negligible photocatalytic activity of Ni-100 (Fig. 9(c)), increasing the ratio of Ni_xS_y in the composite will not only result in a decrease of ZnS amount (note that a fixed amount (20 mg) of mixed sulfides was used for the photocatalysis) but also challenge the light absorption of ZnS. Therefore, the optimal Ni_xS_y molar ratio exists, which was found to be approximately 10 at.% (the actual Ni amount of Ni-20, see Table 1).

Singlet molecular oxygen was previously found in TiO$_2$ photocatalysis by means of near-infrared phosphorescence [35] but we did not succeed in its detection in either ZnS or ZnS-Ni_xS_y composite. We believe that it is due to fast quenching of singlet oxygen because of surface defects of ZnS. We therefore examined photoluminescence of ZnS and ZnS-Ni_xS_y composite and found that all exhibit distinctive photoluminescence attributed to defects states of ZnS (see Supplementary Information, Fig. S5) [36].

To determine main active species in the photocatalytic reaction, trapping experiments were implemented for Ni-0 and Ni-20. The trapping experiments were conducted by adding chemicals that can exclusively consume one of active species for eosin B degradation [37]. Those chemicals are called scavengers and there are several different types—such as scavengers for superoxide radical anions ($^{\cdot}O_2^-$), hydroxyl radicals ($^{\cdot}OH$), and holes (h^+). Among many scavengers, benzoquinone (BQ) is known to be a scavenger for $^{\cdot}O_2^-$, isopropyl alcohol (IPA) for $^{\cdot}OH$, and ammonium oxalate (AMO) for h^+ [38]. Eosin B degradation was performed with Ni-0 and Ni-20 in the presence of those scavengers (Fig. 10). By adding BQ, the catalytic activity of Ni-0 was significantly inhibited while that of IPA had no influence on its catalytic activity. AMO also affected the catalytic activity of Ni-0 but not to the extent that BQ did. A highly similar trend was found in the trapping experiment regarding Ni-20's catalytic activity. The two results indicated that both Ni-0 and Ni-20 share a similar mechanism of photocatalytic function that involves strong reductive decomposition by $^{\cdot}O_2^-$ and moderate oxidative decomposition by h^+. The strong reductive powder of Ni-0 originates from its deep conduction band edge (-1.04 eV for ZnS); hence, it is conceivable that Ni-20 has a similar conduction band position.

A co-catalyst is a metal or metal compound that is loaded onto a semiconductor photocatalyst and functions to enhance its efficiency. Co-catalysts themselves cannot generate charge-carriers (e^- or h^+) by light irradiation but can steer the kinetics of charge-carriers that were built by the semiconductor photocatalyst [39]. Ni or Ni-based compounds recently have drawn attention as a co-catalyst since they are cheap and earth-abundant substitutes of widely used noble metal co-catalysts (Au, Pt, and Pd) [40]. In this respect, it is reasonable to consider that ZnS is a semiconductor photocatalyst in the composite (Ni-20), while Ni_xS_y is a co-catalyst since the addition of Ni_xS_y to ZnS boosts the photocatalytic activity of ZnS while Ni_xS_y alone has no detectable catalytic activity (see Fig. 9(c)).

In addition to organic dye degradation, photocatalytic H$_2$-generation was examined by our sulfide materials. Fig. 11 shows the amount of H$_2$ produced by Ni-0, Ni-20 and Ni-100 under a solar simulator (AM1.5) as a function of time. While almost no H$_2$ was generated by Ni-100, 24.87 ($\pm$ 1.53), and 131.19 ($\pm$ 4.70) μmol $g^{-1}h^{-1}$ of H$_2$ were generated by Ni-0 and Ni-20, respectively. When only visible light or no light was supplied, no H$_2$ was produced for either catalyst. Taking into account that both Ni-0 and Ni-20 have large bandgaps (> 3.65 eV, see Fig. 8(b)) enabling only a small portion of solar simulated light (< 4%) to be absorbed, the amount of H$_2$ production was significant. The
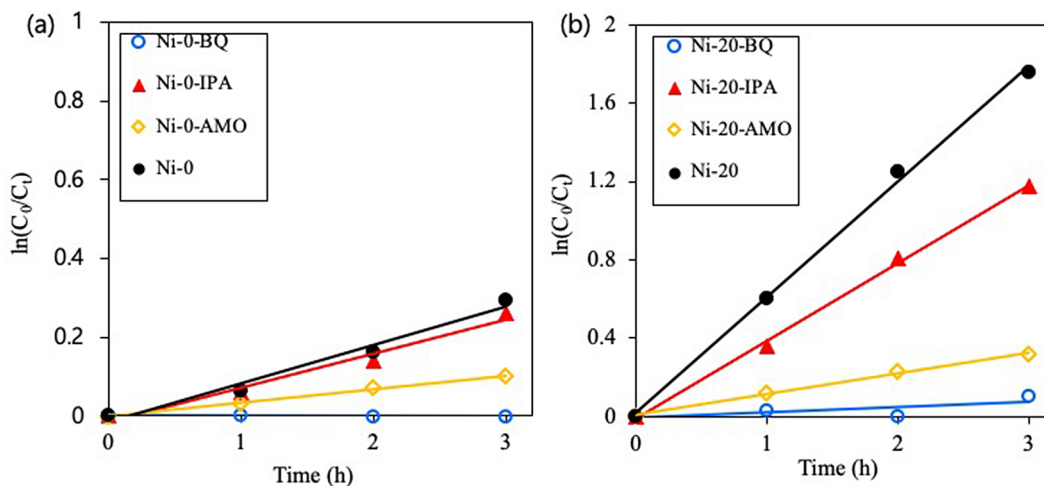

Fig. 10. Scavenger tests for photodegradation of eosin B (a) by Ni-0; (b) by Ni-20 in the presence of benzoquinone (BQ), isopropyl alcohol (IPA), and ammonium oxalate (AMO) [C_o (initial concentration of eosin B) over C_t (concentration of eosin B at the time t)].
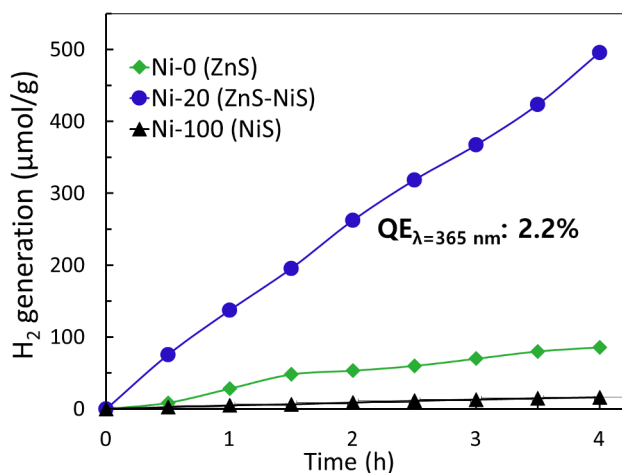
Fig. 11. H$_2$ generation (μmol g^{-1}) as a function of time (h) by Ni-0, Ni-20, and Ni-100.
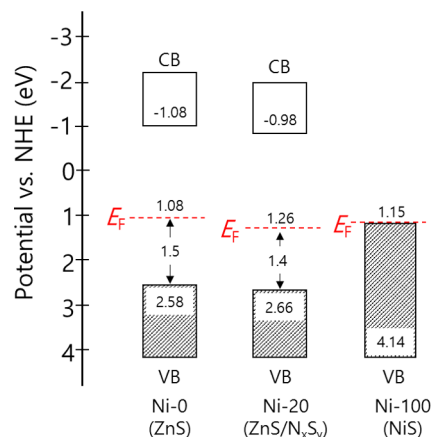

Fig. 12. Band structures of Ni-0, Ni-20, and Ni-100, as measured by XPS and UPS (CB for conduction band; VB for valence band; grey area for filled states; red dashed lines for EF). (For interpretation of the references to color in this figure legend, the reader is referred to the web version of this article.)

reusability test was conducted with Ni-0 and Ni-20 for three cycles and a slight decrease of catalytic activity over each cycle was found (Supplementary Information, Fig. S6). The decrease likely originates from oxidative degradation of the sulfides during exposure to the light. The degradation can be further minimized by an optimal choice of electrolyte solution for efficient scavenging of oxidative species or complete removal of any residual oxygen [1].

The apparent quantum efficiency of Ni-20 toward H$_2$-generation was measured at 365 nm (not the optimal wavelength for light absorption of Ni-20 (see Fig. 8(a) but unavoidable choice due to instrument limitations). The H$_2$-generation under the measurable condition was 80 μmol g^{-1}h^{-1}, accounting for quantum efficiency of 2.2%. In comparison, the reported quantum efficiencies of ZnS and CdS solid solution photocatalysts were 2.17 and 0.60% under UV and visible light irradiation, respectively [13]. Considering the mismatch between the absorption and irradiation wavelengths, the current quantum efficiency of 2.2% is quite high, inferring efficient separation of charge carriers by the heterojunction formation.

Intrigued by the recyclability of Ni-20 towards the hydrogen production, reusability of Ni-0 and Ni-20 for eosin B degradation was tested (Supplementary Information, Fig. S7). For three cycles, the activity of both Ni-0 and Ni-20 was significantly reduced. However, the activity of Ni-20 was maintained during 3–5 cycles while that of Ni-0 kept decreasing. Photo-corrosion of metal sulfide photocatalyst is not unusual in an aerated environment [3]. It is reported that the valence band of ZnS (2.58 eV vs. NHE) is more positive than the oxidation potential of S (0.28 V vs. NHE), and hence h$^+$ generated by ZnS upon illumination corrodes ZnS into zinc sulphate (ZnSO$_x$) [41]. This photo-corrosion of ZnS is often not severe in photocatalytic H$_2$-generation from water, due to the use of an electrolyte solution containing scavengers of an oxidative species (Na$_2$S/Na$_2$SO$_3$) [1]. Nonetheless, we observed the activity of Ni-20 to be sustained for up to 5 cycles. It has been reported that the photo-corrosion of ZnS can be suppressed by engineering its valence band (VB) position to be less positive vs. NHE through the formation of defect states or doping levels, thereby weakening the oxidative capability of h$^+$ [42–44]. For example, Zhou et al. reported N-doped ZnS as a stable photocatalyst and argued that N-doping created a narrow acceptor level above the valence band position of ZnS, helping to enhance its stability [41]. Therefore, it is reasonable to assume that the initial decrease originates from ZnS-single component parts of Ni-20 that are susceptible to the photo-corrosion, while the sustained activity for 3–5 cycles is attributable to its heterojunction parts in which the oxidative capability of h$^+$ is weakened.

To explain reasons for the enhanced photocatalytic activity and stability of Ni-20, we considered a band alignment of two sulfides.

Valence band spectra of Ni-0, Ni-20 and Ni-100 were obtained by XPS (Supplementary Information, Fig. S8), showing that the valence band edges of Ni-0, Ni-20 and Ni-100 were 1.5, 1.4, and 2.99 eV, respectively. The work function (φ) of each sulfide was obtained from UPS spectra (Supplementary Information, Fig. S9), exhibiting 1.08, 1.26 and 1.15 eV vs. NHE for Ni-0, Ni-20 and Ni-100, respectively. Therefore, valence band edges were determined to be 2.58, 2.66 and 4.14 eV (vs. NHE) respectively. Using bandgaps measured in Fig. 7(b) (3.66 eV for Ni-0 and 3.64 eV for Ni-20), the conduction band edges of Ni-0 and Ni-20 were calculated to be −1.08 and −0.98 eV (vs. NHE), respectively. Since Ni-100 has a metal-like band structure, energy levels below Fermi level (EF) was considered an occupied state. The band structure of each sulfide is presented in Fig. 12, according to the values measured above.

ZnS/We then closely examined the heterojunction via DFT calculation. Since XRD and XPS analysis showed several oxidation states of Ni in Ni$_x$S$_y$ (+2 ~ +4) (see Fig. 3 and Fig. S2), NiS and NiS$_2$ phases (Ni oxidation state = +2 and +4, respectively) were representatively chosen for the calculation. Four different ZnS/Ni$_x$S$_y$ junctions—(a) c-ZnS/c-NiS; (b) c-ZnS/a-NiS; (c) c-ZnS/c-NiS$_2$; and (d) c-ZnS/a-NiS$_2$—were considered for the density of states (DOS) calculation (Fig. 13). The valence band maximum (VBM) of the ZnS in the ZnS/NiS heterojunction was determined to be at 1.80 eV (c-NiS) and 1.27 eV (a-NiS), while that in the ZnS/NiS$_2$ heterojunction was at 0.91 eV (c-NiS$_2$) and 0.50 eV (a-NiS$_2$) ZnS/below the Fermi level. To draw a band diagram of the ZnS and Ni$_x$S$_y$ heterojunctions, the measured energy level of the valence band edge for ZnS (2.58 eV from NHE) was used, and all other energy levels were calculated based on theoretical bandgaps, work functions, and Fermi levels in single crystals. Using the calculated positions for NiS and NiS$_2$ Fermi levels as well as a Schottky-type junction with downward band bending, the band diagram in Fig. 14(a) was generated. Upon excitation of ZnS, photo-generated electrons accumulate on the ZnS side, and holes transfer to the Ni$_x$S$_y$. Under the aerated conditions, the excited electrons reduce O$_2$ to ·O$_2^-$, which reductively degrades eosin B; whereas, in a de-aerated state, they reduce water to H$_2$. On the other hand, holes transferred to the Ni$_x$S$_y$ are directly involved in the oxidative decomposition of eosin B (the literature value for eosin B's oxidative potential is 1.02 eV vs. NHE [9,45]) or consumed by hole scavengers in the H$_2$ production system [1] (Fig. 14(b)). Hydroxyl radicals are difficult to generate because the oxidation potential of hydroxide ions (1.99 eV) is higher than the Fermi levels of Ni$_x$S$_y$, which is highly consistent with our trapping experiments.

This mechanism suggests that the Ni$_x$S$_y$ phase functions as a co-catalyst of the ZnS, serving to help separate the electrons and holes that are generated by ZnS photoabsorption. An electron transfer from the
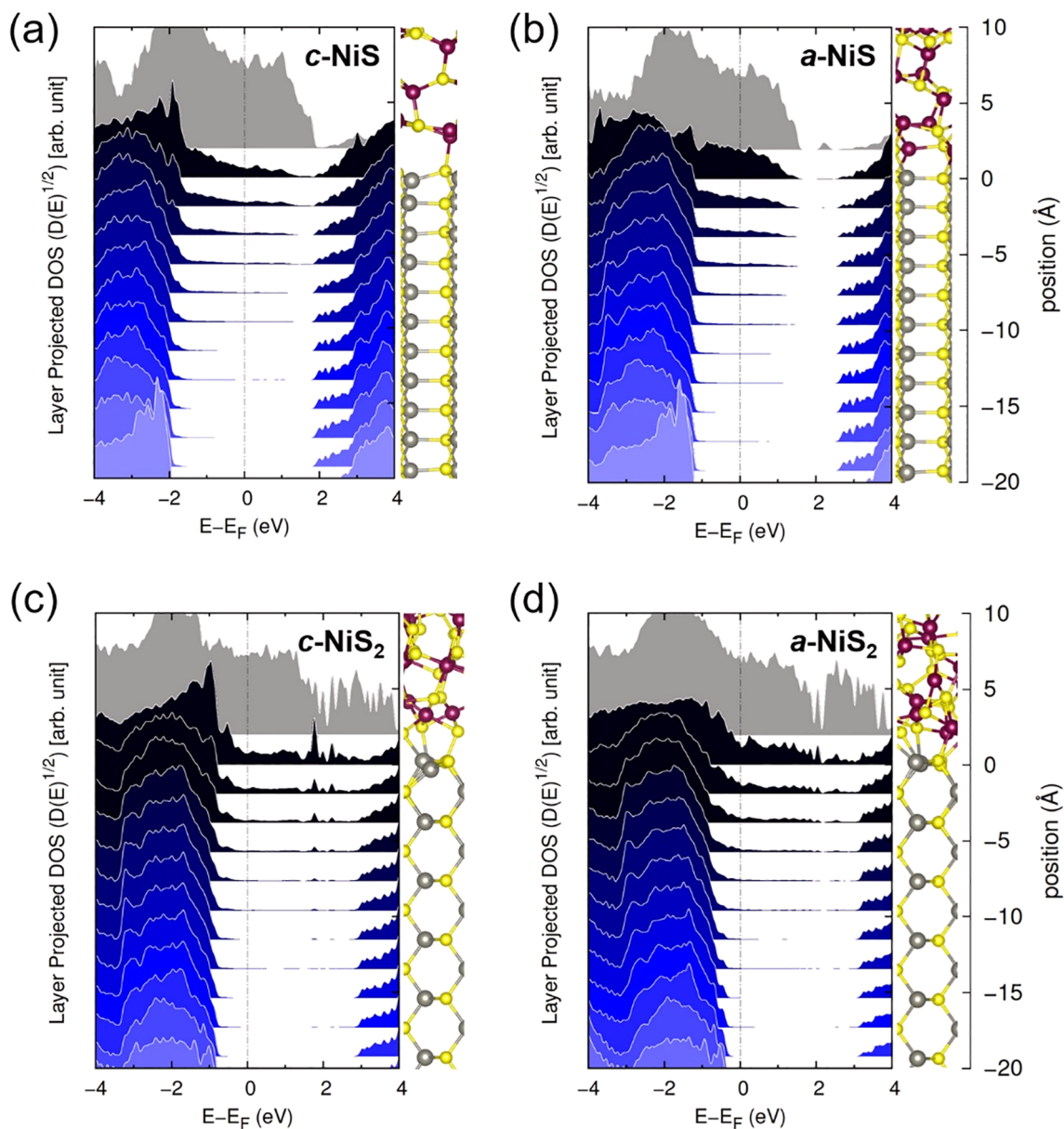
Fig. 13. Electron density of states (DOS) projected onto each layer of (a) *c*-NiS, (b) *a*-NiS (c) *c*-NiS$_2$ and (d) *a*-NiS$_2$ with a *c*-ZnS (1 1 0) surface. Note that VBMs of ZnS locate at (a) 1.80, (b) 1.27 eV, (c) 0.91 and (d) 0.50 eV below the Fermi level (EF).
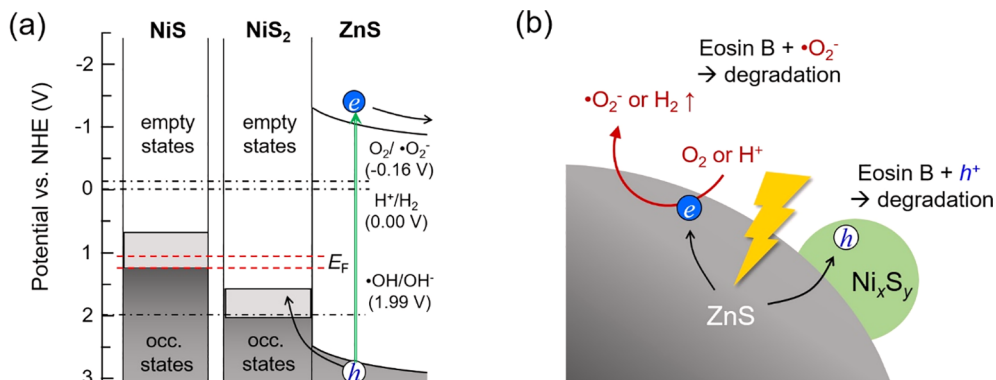

Fig. 14. (a) A band diagram drawn using the VBM level of ZnS relative to E_F from DFT simulations and measured band edges of NiS (paled grey boxes) and (b) suggested mechanisms of eosin B degradation.

conduction band maximum (CBM) of ZnS to the empty states of Ni_xS_y, which may well degrade the activity, is potentially suppressed due to band bending at the Schottky contact. Similar mechanisms have been reported for NiS deposited on different semiconductors, such as TiO_2 [46], and CdS [47], where NiS serves as a co-catalyst by accepting holes from the semiconductor. Ni-based co-catalysts have recently been considered as a suitable substitute for noble metal co-catalysts such as Au, Pt, and Pd, since they have multiple oxidation states and are able to form complexes with many different materials [40].

4. Conclusion

Applying immiscibility and different growth rates of two sulfides, we successfully synthesized ready-to-use ZnS/Ni_xS_y composites by a one-pot hydrothermal method. Along with DFT calculations, kinetic studies, physical analysis of the sulfide composites by XRD, TEM and UV–visible absorption demonstrated that ZnS/Ni_xS_y does not make a solid solution but, instead, form well separated heterojunctions over a wide relative compositional range of Ni to Zn (up to 18%). The ZnS/Ni_xS_y composites showed superior photocatalytic activities when compared to the single component ZnS and Ni_xS_y for both eosin B degradation and hydrogen generation. Our calculated band diagram revealed that the ZnS/Ni_xS_y interface drives charge-carrier separation and that Ni_xS_y functions as a co-catalyst. This study also demonstrates a guideline to synthesize well-made heterojunction of two materials; two materials need to be immiscible, and faster nucleation and growth of host material (ZnS for this study) than guest material is desired.

Declaration of Competing Interest

The authors declare that they have no known competing financial interests or personal relationships that could have appeared to influence the work reported in this paper.

Acknowledgement

Appendix A. Supplementary data

Supplementary data to this article can be found online at https://doi.org/10.1016/j.cej.2020.125092.

References

[1] J.F. Reber, K. Meier, Photochemical production of hydrogen with zinc-sulfide suspensions, J. Phys. Chem. 88 (1984) 5903–5913.

[2] X. Fang, T. Zhai, U.K. Gautam, L. Li, L. Wu, Y. Bando, D. Golberg, ZnS nanostructures: from synthesis to applications, Prog. Mater. Sci. 56 (2011) 175–287.

[3] A. Kudo, Y. Miseki, Heterogeneous photocatalyst materials for water splitting, Chem. Soc. Rev. 38 (2009) 253–278.

[4] K. Ozawa, M. Emori, S. Yamamoto, R. Yukawa, S. Yamamoto, R. Hobara, K. Fujikawa, H. Sakama, I. Matsuda, Electron-hole recombination time at TiO_2 single-crystal surfaces: influence of surface band bending, J. Phys. Chem. Lett. 5 (2014) 1953–1957.

[5] L. Li, P.A. Salvador, G.S. Rohrer, Photocatalysts with internal electric fields, Nanoscale 6 (2014) 24–42.

[6] X. Wang, Q. Xu, M. Li, S. Shen, X. Wang, Y. Wang, Z. Feng, J. Shi, H. Han, C. Li, Photocatalytic overall water splitting promoted by an α–β phase junction on Ga_2O_3, Angew. Chem. Inter. Ed. 51 (2012) 13089–13092.

[7] J.L. Shi, On the synergetic catalytic effect in heterogeneous nanocomposite catalysts, Chem. Rev. 113 (2013) 2139–2181.

[8] M. Saruyama, S. Kim, T. Nishino, M. Sakamoto, M. Haruta, H. Kurata, S. Akiyama, T. Yamada, K. Domen, T. Teranishi, Phase-segregated $NiP_x@FeP_yO_z$ core@shell nanoparticles: ready-to-use nanocatalysts for electro- and photo-catalytic water oxidation through in situ activation by structural transformation and spontaneous ligand removal, Chem. Sci. 9 (2018) 4830–4836.

[9] L. Shao, D. Jiang, P. Xiao, L. Zhu, S. Meng, M. Chen, Enhancement of g-C_3N_4 nanosheets photocatalysis by synergistic interaction of ZnS microsphere and RGO inducing multistep charge transfer, Appl. Catal. B: Environ. 198 (2016) 200–210.

[10] M.-K. Lee, T.-H. Shih, High photocatalytic activity of nanoscaled heterojunction of ZnS grown on fluorine and nitrogen Co–doped TiO_2, J. Electrochem. Soc. 154 (2007) P49–P51.

[11] S. Chaguetmi, F. Mammeri, S. Nowak, P. Decorse, H. Lecoq, M. Gaceur, J.B. Naceur, S. Achour, R. Chtourou, S. Ammar, Photocatalytic activity of TiO_2 nanofibers sensitized with ZnS quantum dots, RSC Adv. 3 (2013) 2572–2580.

[12] C. Mondal, A. Singh, R. Sahoo, A.K. Sasmal, Y. Negishi, T. Pal, Preformed ZnS nanoflower prompted evolution of CuS/ZnS p–n heterojunctions for exceptional visible-light driven photocatalytic activity, New J. Chem. 39 (2015) 5628–5635.

[13] C.J. Xing, Y.J. Zhang, W. Yan, L.J. Guo, Band structure-controlled solid solution of $Cd_{1-x}Zn_xS$ photocatalyst for hydrogen production by water splitting, Inter. J. Hydrogen Energy 31 (2006) 2018–2024.

[14] L. Hao, F.-Q. Bai, C.-P. Kong, S. Bibi, H.-X. Zhang, Theoretical studies of heteroatom-doping in TiO_2 to enhance the electron injection in dye-sensitized solar cells, RSC Adv. 5 (2015) 79868–79873.

[15] K. Li, R. Chen, S.-L. Li, M. Han, S.-L. Xie, J.-C. Bao, Z.-H. Dai, Y.-Q. Lan, Self-assembly of a mesoporous ZnS/mediating interface/CdS heterostructure with enhanced visible-light hydrogen-production activity and excellent stability, Chem. Sci. 6 (2015) 5263–5268.

[16] S. Kumar, C. Chen, C. Dong, Y. Ho, J. Lee, T. Chan, R. Thangavel, T. Chen, B. Mok, S. Rao, Room temperature ferromagnetism in Ni doped ZnS nanoparticles, J. Alloys Compd. 554 (2013) 357–362.

[17] A. Kudo, M. Sekizawa, Photocatalytic H_2 evolution under visible light irradiation on Ni-doped ZnS photocatalyst, Chem. Commun. 1371–1372 (2000).

[18] H. Derikvandi, A. Nezamzadeh-Ejhieh, Comprehensive study on enhanced photocatalytic activity of heterojunction ZnS-NiS/zeolite nanoparticles: Experimental design based on response surface methodology (RSM), impedance spectroscopy and GC-MASS studies, J. Colloid Interf. Sci. 490 (2017) 652–664.

[19] C. Wei, C. Cheng, J. Zhao, Z. Wang, H. Wu, K. Gu, W. Du, H. Pang, Mesoporous ZnS–NiS nanocomposites for nonenzymatic electrochemical glucose sensors, Chem. Open 4 (2015) 32–38.

[20] D.C. Jiang, L. Zhu, R.M. Irfan, L. Zhang, P.W. Du, Integrating noble-metal-free NiS cocatalyst with a semiconductor heterojunction composite for efficient photocatalytic H_2 production in water under visible light, Chinese. J. Catal. 38 (2017) 2102–2109.

[21] J.P. Perdew, K. Burke, M. Ernzerhof, Generalized gradient approximation made simple, Phys. Rev. Lett. 77 (1996) 3865–3868.

[22] L.G. Ferreira, M. Marques, L.K. Teles, Approximation to density functional theory for the calculation of band gaps of semiconductors, Phys. Rev. B 78 (2008) 125116.

[23] J. Doumont, F. Tran, P. Blaha, Limitations of the DFT-1/2 method for covalent semiconductors and transition-metal oxides, Phys. Rev. B 99 (2019).

[24] K.H. Xue, J.H. Yuan, L.R.C. Fonseca, X.S. Miao, Improved LDA-1/2 method for band structure calculations in covalent semiconductors, Comp. Mater. Sci. 153 (2018) 493–505.

[25] J.M. Soler, E. Artacho, J.D. Gale, A. García, J. Junquera, P. Ordejón, D. Sánchez-Portal, The SIESTA method for ab initio order-N materials simulation, J. Phys.: Condens. Matter 14 (2002) 2745.

[26] R. Karthikeyan, M. Navaneethan, J. Archana, D. Thangaraju, M. Arivanandhan, Y. Hayakawa, Shape controlled synthesis of hierarchical nickel sulfide by the hydrothermal method, Dalton Trans. 43 (2014) 17445–17452.

[27] S. Khan, H. Cho, D. Kim, S.S. Han, K.H. Lee, S.-H. Cho, T. Song, H. Choi, Defect engineering toward strong photocatalysis of Nb-doped anatase TiO_2: Computational predictions and experimental verifications, Appl. Catal. B: Environ. 206 (2017) 520–530.

[28] J.M. Buriak, P.V. Kamat, K.S. Schanze, Best practices for reporting on heterogeneous photocatalysis, ACS Appl. Mater. Inter. 6 (2014) 11815–11816.

[29] A.K. Kole, P. Kumbhakar, Cubic-to-hexagonal phase transition and optical properties of chemically synthesized ZnS nanocrystals, Results Phys. 2 (2012) 150–155.

[30] Y.X. Huang, M. Cheng, Z.C. Xiang, Y.M. Cui, Facile synthesis of $NiCo_2S_4$/CNTs nanocomposites for high-performance supercapacitors, Roy. Soc. Open Sci. 5 (2018).

[31] C. Buchmaier, M. Glanzer, A. Torvisco, P. Poelt, K. Wewerka, B. Kunert, K. Gatterer, G. Trimmel, T. Rath, Nickel sulfide thin films and nanocrystals synthesized from nickel xanthate precursors, J. Mater. Sci. 52 (2017) 10898–10914.

[32] G. Wang, B. Huang, Z. Li, Z. Lou, Z. Wang, Y. Dai, M.-H. Whangbo, Synthesis and characterization of ZnS with controlled amount of S vacancies for photocatalytic H_2 production under visible light, Sci. Rep. 5 (2015) 8544.

[33] J. Huang, Z. Shi, X. Dong, Nickel sulfide modified TiO_2 nanotubes with highly efficient photocatalytic H_2 evolution activity, J. Energ. Chem. 25 (2016) 136–140.

[34] L. Zhang, B. Tian, F. Chen, J. Zhang, Nickel sulfide as co-catalyst on nanostructured TiO_2 for photocatalytic hydrogen evolution, Inter. J. Hydrogen Energy 37 (2012) 17060–17067.

[35] T. Daimon, Y. Nosaka, Formation and behavior of singlet molecular oxygen in TiO_2 photocatalysis studied by detection of near-infrared phosphorescence, J. Phys. Chem. C 111 (2007) 4420–4424.

[36] B. Poornaprakash, D.A. Reddy, G. Murali, N.M. Rao, R.P. Vijayalakshmi,

B.K. Reddy, Composition dependent room temperature ferromagnetism and PL intensity of cobalt doped ZnS nanoparticles, J. Alloys Compd 577 (2013) 79–85.

[37] P. Pattanaik, M.K. Sahoo, TiO_2 photocatalysis: progress from fundamentals to modification technology, Desalin. Water Treat. 52 (2014) 6567–6590.

[38] W.J. Li, D.Z. Li, J.X. Wang, Y. Shao, J.M. You, F. Teng, Exploration of the active species in the photocatalytic degradation of methyl orange under UV light irradiation, J. Mol. Catal. A-Chem. 380 (2013) 10–17.

[39] S. Bai, W.J. Yin, L.L. Wang, Z.Q. Li, Y.J. Xiong, Surface and interface design in cocatalysts for photocatalytic water splitting and CO_2 reduction, Rsc. Adv. 6 (2016) S7446–S7463.

[40] Y. Xu, R. Xu, Nickel-based cocatalysts for photocatalytic hydrogen production, Appl. Surf. Sci. 351 (2015) 779–793.

[41] Y.S. Zhou, G. Chen, Y.G. Yu, Y.J. Feng, Y. Zheng, F. He, Z.H. Han, An efficient method to enhance the stability of sulphide semiconductor photocatalysts: a case study of N-doped ZnS, Phys. Chem. Chem. Phys. 17 (2015) 1870–1876.

[42] X.Q. Hao, Y.C. Wang, J. Zhou, Z.W. Cui, Y. Wang, Z.G. Zou, Zinc vacancy-promoted photocatalytic activity and photostability of ZnS for efficient visible-light-driven hydrogen evolution, Appl. Catal. B-Environ. 221 (2018) 302–311.

[43] J.Z. Su, Y.K. Wei, L. Vayssieres, Stability and performance of sulfide-, nitride-, and phosphide-based electrodes for photocatalytic solar water splitting, J. Phys. Chem. Lett. 8 (2017) 5228–5238.

[44] T. Mahvelati-Shamsabadi, E.K. Goharshadi, Photostability and visible-light-driven photoactivity enhancement of hierarchical ZnS nanoparticles: the role of embedment of stable defect sites on the catalyst surface with the assistant of ultrasonic waves, Ultrason. Sonochem. 34 (2017) 78–89.

[45] K. Fidaly, C. Ceballos, A. Falguieres, M.S.I. Veitia, A. Guy, C. Ferroud, Visible light photoredox organocatalysis: a fully transition metal-free direct asymmetric alpha-alkylation of aldehydes, Green Chem. 14 (2012) 1293–1297.

[46] M. Mollavali, C. Falamaki, S. Rohani, High performance NiS-nanoparticles sensitized TiO2 nanotube arrays for water reduction, Inter. J Hydrogen Energy 41 (2016) 5887–5901.

[47] J. Zhang, S.Z. Qiao, L.F. Qi, J.G. Yu, Fabrication of NiS modified CdS nanorod p-n junction photocatalysts with enhanced visible-light photocatalytic H-2-production activity, Phys. Chem. Chem. Phys. 15 (2013) 12088–12094.